PAPER

Perfectly conducting graphene electronic waveguide with curved channels

IOP Publishing Journal of Physics: Condensed Matter
J. Phys.: Condens. Matter **30** (2018) 325301 (8pp) https://doi.org/10.1088/1361-648X/aacfca

Perfectly conducting graphene electronic waveguide with curved channels

Vahid Mosallanejad[1], Ke Wang[2,3], Zhenhua Qiao[2,3] and Guoping Guo[1]

[1] CAS Key Laboratory of Quantum Information, and Synergetic Innovation Center of Quantum Information and Quantum Physics, University of Science and Technology of China, Chinese Academy of Sciences, Hefei 230026, People's Republic of China
[2] ICQD, Hefei National Laboratory for Physical Sciences at Microscale, and Synergetic Innovation Center of Quantum Information and Quantum Physics, University of Science and Technology of China, Hefei, Anhui 230026, People's Republic of China
[3] CAS Key Laboratory of Strongly-Coupled Quantum Matter Physics and Department of Physics, University of Science and Technology of China, Hefei, Anhui 230026, People's Republic of China

E-mail: qiao@ustc.edu.cn and gpguo@ustc.edu.cn

Received 26 March 2018, revised 20 June 2018
Accepted for publication 28 June 2018
Published 17 July 2018

Abstract

We theoretically investigate the electronic transport properties of curved graphene waveguides by employing non-equilibrium Green's function techniques. We systematically study the dependence of the confined waveguide modes on the potential difference, the width of waveguide and side barrier. Through two-terminal electronic transport calculations, we show that the conductance of confined waveguide modes is rather robust against the bending degree of waveguide, in consistence with the band insensitivity to the side barrier. This finding of the perfectly conducting channels strongly suggests the possibility of applying the graphene waveguide in the design of low-power nanoelectronics.

Keywords: electronic transport, graphene, electronic waveguide

(Some figures may appear in colour only in the online journal)

1. Introduction

Due to its linear Dirac dispersion, graphene exhibits excellent physical properties, including the electronic and optical aspects [1–3]. All these made graphene a promising candidate for designing future electronics. However, the intrinsic zero-gap of graphene hindered the possibility of replacing silicon to realize the basic on/off function of semiconductors. Subsequent efforts have been made to explore various two-dimensional (2D) materials that naturally harbour bulk band gaps, e.g. silicene [4] and transition metal dichalcogenide MX_2 [5]. Although a variety of new 2D materials become constantly proposed in theory and discovered in the experiment, high mobility of graphene at room temperature [6] has attracted overwhelming attention. Both theoretical and experimental researchers continue exploiting graphene-based electronics via external manipulation after a dozen years ever since its first experimental discovery.

Two-component wavefunction in graphene, so-called pseudospin, results in extraordinary tunneling phenomena, namely Klein tunneling [7]. This phenomenon is in close conjunction with suppression of backscattering in graphene and responsible for the high mobility in the single-layer graphene lattice. In the presence of uniform potential well i.e. confined regime, however, the equation of motion can be reduced to an Eigen-value equation that resembles the Helmholtz equation in optics [8]. In particular, optic-like phenomena such as Goos–Hanchen and Veselago lens effects, have been studied in graphene [9–11]. Extensive theoretical calculations have been carried out to investigate electronic modes in graphene waveguide by solving Dirac–Weyl equation [12–18]. As a result, the separation of several waveguide modes from the other conic subbands (corresponding to barriers modes) and sporadic conversion of valance subbands to the conduction subbands, are observed. It has commonly been assumed that the transport through graphene waveguide can be classified

into two regimes: (1) The optical waveguide regime, often called total reflection regime, which can occur when the barriers and waveguide have the same polarity; (2) p-n guiding regime, where the polarity of carriers between barriers and waveguide are different [19, 20]. Confinement of carriers in a n-p-n junction is demonstrated in latest experimental studies [21, 22]. Furthermore, kinked graphene waveguide based on graphene antidot has been proposed [23]. Exotic phenomena, such as snake states, have been realized in graphene p-n junction [24–26]. Most interestingly, recent experimental and theoretical studies have shown the valley-degenerate transport in graphene waveguide with arbitrary chiral orientation, except armchair edge [27, 29].

Theoretically, graphene waveguide [19, 29] can be achieved by externally applying a hard-wall square-shape potential well in the transverse direction (see figure 1(a)). This should be experimentally feasible with recent advances in the fabrication techniques and applying thin film insulators (e.g. hexagonal boron nitride). So far, both theoretical and experimental studies have been mainly concentrated on the straight graphene waveguides. Moreover, the ballistic transport of the confined states in the quantum well has been experimentally demonstrated [19, 20]. It is well-known that one of the most striking features of optical fibers is that the electromagnetic waves can efficiently transmit in any kinds of bending. This is directly applied in the field of information communication. Analogous to a bending optical fiber [30], it is interesting to explore whether or not the curved graphene waveguide can have application prospects in nano-sized integrated systems and electronic interferometry.

In this article, we investigate the electronic transport properties of curved graphene waveguides by employing Green's function techniques. Graphene waveguides can be readily prepared by applying an external electric gate along a finite-sized graphene nanoribbon within the graphene flake. We systematically investigate the dependence of the confined waveguide modes on the potential difference ΔV, the width of waveguide $W_{\rm G}$ and the width of the side barrier $W_{\rm B}$. It shows that the electronic structures are insensitive to the variation of the width of side barrier $W_{\rm B}$. Tunable graphene waveguides can be realized by adjusting the external gate voltage. Through a two-terminal electronic transport calculation, we find that the nearly quantized conductance (ballistic transport) is quite robust against the bending degree of waveguide, in consistence with the band insensitivity to the width of side barrier. In present work, we have observed the signature of valley transport for ultra-thin graphene waveguide with armchair edge. Our findings strongly demonstrate the possibility of designing the graphene-waveguide based low-power nanoelectronics.

2. Tight-binding model

In our studies, we consider the armchair graphene nanoribbons, where valleys K and K' are mixed and indistinguishable. Figures 1(a) and (b) display respectively the schematic plots of straight and curved graphene waveguides, where the confined potential ΔV is applied at the blue colored atomic sites.

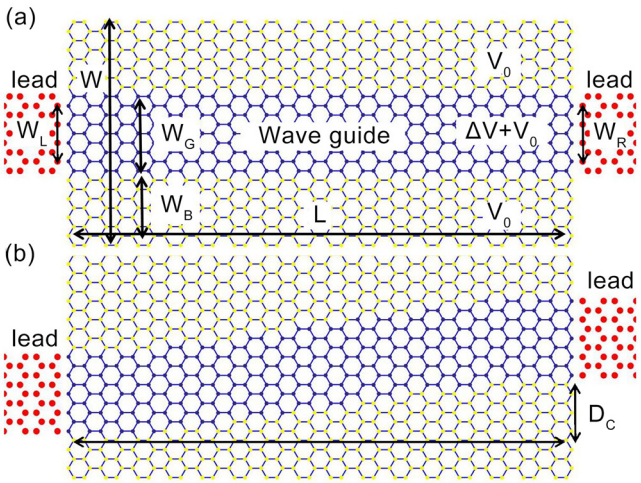

Figure 1. Schematic plots of (a) straight and (b) curved waveguides in armchair graphene nanoribbons, being connected with left and right leads extended from the waveguides. Blue atoms label the graphene waveguide. W, $W_{\rm L,R}$, $W_{\rm G}$ and $W_{\rm B}$ indicate the widths of graphene nanoribbon, left or right terminals, waveguide and side barriers, respectively. L represents the device length. ΔV is the potential difference between waveguide and barriers, and V_0 is the on-site potential in both side barriers. $D_{\rm C}$, the relative shift between left and right terminals, characterizes the degree of bending in curved waveguides.

The π-orbital tight-binding model Hamiltonian of graphene in the presence of gate voltage can be written as:

$$H = -t\sum_{\langle ij\rangle} a_i^{\dagger}a_j + \sum_i v_i a_i^{\dagger}a_i, \tag{1}$$

where $a_i^{\dagger}$ and a_i are the creation and annihilation operators at ith atomic site, respectively. v_i is the on-site potential energy, which is set to be zero for reference at the side barrier region and ΔV in the waveguide region. The nearest-neighbor hopping energy is set to be $t = 2.78$ eV. Due to the relatively large width of the system considered, extra Hamiltonian modification for the edge states or other imperfections is not included [32, 33].

3. Band structure of graphene waveguide

Band structure can usually provide fundamental information to understand the electronic transport properties. By exactly diagonalizing the tight-binding Hamiltonian of the graphene nanoribbon, the band structure can be obtained. Figure 2(a) displays the band structure of armchair ribbon with a well-known conic-shape subbands encapsulated in the celebrated Dirac conicband of bulk graphene $E(k_x) = \pm\hbar\nu_{\rm F}|k_x|$.

In the standard convention, AGNRs can defined by N-AGNR where N is the number of dimer lines. Based on crystal structure of graphene, N is related to the width of AGNR, W, via $W = N\frac{\sqrt{3}}{2}a$, where $a = 0.142$ nm is the carbon–carbon bond length. Throughout of this work we employ this relation to establish a connection between different widths and dimer lines which are essential inputs for the numerical code. Here, each supercell includes 818 atoms, corresponding to a width about $W = 50.4$ nm. By applying a

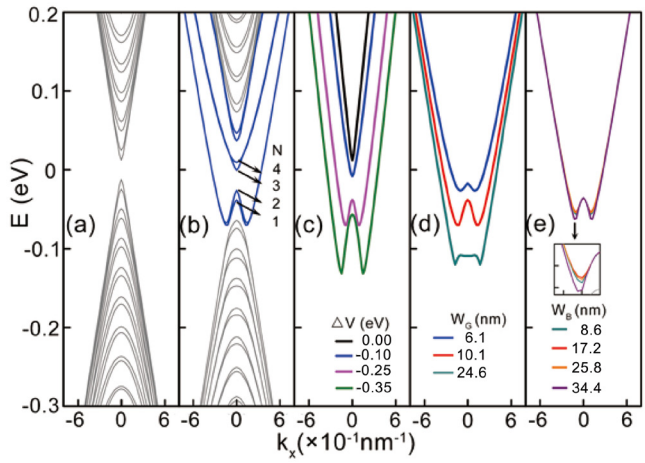

Figure 2. (a) Band structure of armchair nanoribbon with a width of $W = 50.4$ nm, with the supercell including 818 atoms. (b) Band structure of armchair nanoribbon harboring a waveguide as displayed in the central region of figure 1(a), where $W_G = 10.1$ nm and $\Delta V = -0.25$ eV. The blue bands indicate the modes arising from the waveguide. (c) Relative shift of the first subband due to the variation of ΔV in the waveguide. (d) First subband mode dispersion for different waveguide thickness W_G. (e) First subband dispersion for different widths of barriers W_B. In (c) and (d), the parameters are the same as those in panel (b) except the varying parameter.

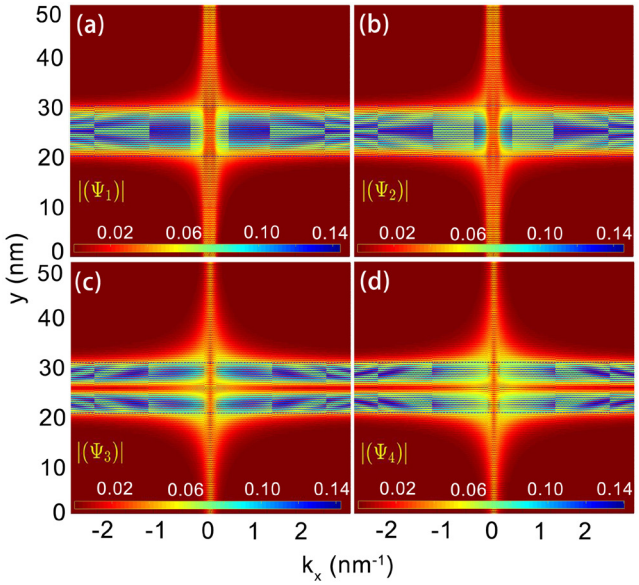

Figure 3. Spatial distribution plot of the wavefunctions across the armchair ribbon as a function of k_x for the first four bands as highlighted in figure 2(b). One can see that all the bands are confined inside the waveguide region except the k_x points close to 0. The parameters are respectively $W = 50.4$ nm, $W_G = 10.1$ nm, and $\Delta V = -0.25$ eV. Dashed white lines are inserted to identify the boundaries of the quantum well or waveguide.

gate voltage of $\Delta V = -0.25$ eV at the region of $W_G = 10.1$ nm inside the armchair ribbon, a graphene waveguide is produced and the resulting bands are displayed in figure 2(b). One can observe that the confined modes in blue arise and their mixture with the valence bands results in the asymmetry between the conduction and valence bands in the low-energy region. In below, we show that they are localized inside the graphene waveguide.

Then, we investigate the evolution of confined waveguide modes as a function of the applied gate voltage ΔV. Figure 2(c) displays the first conduction subband variation along with the increase of ΔV. One can find that for a relatively small potential, e.g. $\Delta V = -0.10$ eV, the first conduction subband moves downward; for large potentials exceeding the critical point, e.g. $\Delta V = -0.25$ eV and -0.35 eV, the first conduction band becomes overlapped with the valence bands, leading to a band inversion. Figure 2(d) displays the evolution of the first conduction band for different waveguide widths $W_G = 6.1, 10.1,$ and 24.6 nm at fixed $\Delta V = -0.25$ eV. One can find that for narrower waveguide, the band inversion occurs at the position close to the charge neutrality point; while for wider waveguide, the band inversion occurs at the energy farther away from the charge neutrality point, therefore giving rise to a wider energy interval for ballistic transport. Figure 2(e) displays the dependence of the first conduction band on the width of the side barrier W_B. One can clearly observe that the confined waveguide modes are insensitive to the variation or asymmetry of the width of side barrier W_B (see inset of the panel (e) for magnification of small variation). Therefore, our exploration in figure 2(e) indicates that the confined subbands are insensitive to the ribbon width, beyond the dispersive area with the conduction subbands exhibiting negative slopes. This suggests the possible existence of perfectly conducting (i.e. ballistic transport) energy channels in a graphene waveguide subjected to proper potential wells.

To show how the waveguide modes are distributed in the potential well, in figure 3 we plot the spatial wavefunction distribution across the armchair ribbon at different wavevectors for the four subbands labelled in figure 2(b). For clear comparison, two horizontal white color dashed lines are inserted to identify the boundaries of the quantum well or waveguide. Surprisingly, one can clearly see that most of the confined waveguide modes for wave vectors away from $k_x = 0$ are perfectly confined inside the waveguide; while the remaining parts are not localized inside the waveguide but distributed in the whole range of the ribbon. This is distinct from the topologically protected edge modes that are completely localized at the system boundaries therefore robust against various external disorders.

In a practical device, the potential well across an armchair supercell, a cross-section on transverse direction of figure 1, is usually not a perfect hard-wall profile and often exhibits certain smooth variation between the barrier and the well [15]. Thus, it is essential to characterize conducting energy channels in the presence of edge smoothness. For comparison, two types of potential profiles have been considered: a wider hard-wall waveguide of $W_G = 20.2$ nm and a smooth edge waveguide with full width half maximum (FWHM) being equal to W_G, as displayed in upper panels of figures 4(a) and (b). The corresponding band structures are plotted in lower panels of figures 4(c) and (d). Comparison between band structures reveals that waveguide modes do not change substantially when a hard-wall potential profile is replaced by a soft edge potential well. Moreover, we also plot the waveguide modes

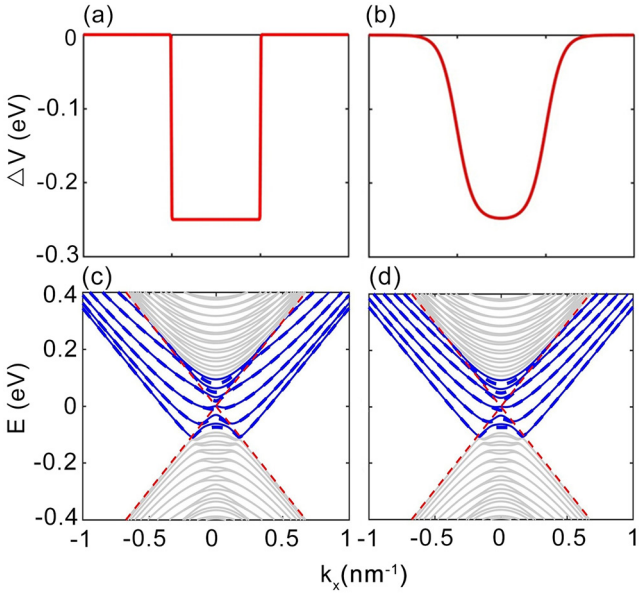

Figure 4. (a) and (b) Two type of potential profiles across an armchair ribbon supercell. (c) and (d) Corresponding bandstructures are plotted right under each potential profiles. The parameters are respectively $W = 60.5$ nm, $W_G = 20.2$ nm, and $\Delta V = -0.25$ eV. Dashed red lines are the Dirac conicbands of infinite graphene $E(k_x) = \pm\hbar v_F|k_x|$.

for a supercell system with $W = 80.7$ nm and $W_G = 40.3$ nm in figure 5. Waveguide modes are plotted for two different depths of potential well, namely $\Delta V = -0.25$ eV and $\Delta V = -0.13$ eV in figures 5(a) and (b), respectively. The edge of potential is smooth as plotted in figure 4(b). The waveguide bands are highlighted in blue, and degenerate bands are separated by solid and dashed lines. In the following section, we try to understand the transport properties in a wider graphene nanoribbon by analyzing the conducting bands of a wider armchair supercell. Consequently, we observe that the wider waveguides provide more conducting channels, and the valley degeneracy is still preserved.

4. Electronic transport in curved waveguides

To explore the robustness of the confined waveguide modes against the bending degree of the graphene waveguide, we use a two-terminal mesoscopic setup to study the conductance as a function of the Fermi level E_F for different bending degrees D_C. The two terminal conductance $G(E)$ is expressed as

$$G = \frac{2e^2}{h}\mathrm{Tr}[\Gamma_L G^r \Gamma_R G^a], \qquad (2)$$

where $\Gamma_{L,R}$ are the line-width functions coupling the left and right terminals with the central scattering region [31]. Here, the coefficient '2' represents the spin degree of freedom. The retarded Green function G^r is defined as $G^r = [(E + i\eta) - H - \Sigma_L - \Sigma_R]^{-1}$ with $G^a = (G^r)^\dagger$. The open boundary condition of the left and right terminals is implemented via $\Gamma_{L,R} = i(\Sigma^r_{L,R} - \Sigma^a_{L,R})$, where $\Sigma^a_{L,R} = (\Sigma^r_{L,R})^\dagger$. Terms $\Sigma_{L,R}$ are respectively self-energies of the semi-infinite left and right terminals [34, 35]. To effectively examine the robustness of the confined waveguide modes of the curved graphene waveguide, one has to ensure that the terminals can better match the central scattering region to avoid the strong back-scattering.

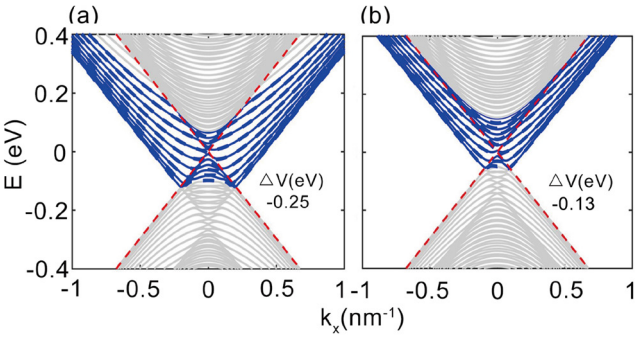

Figure 5. Bandstructures for wider waveguide. The system parameters are set to be $W = 80.7$ nm and $W_G = 40.3$ nm. (a) $\Delta V = -0.25$ eV; (b) $\Delta V = -0.13$ eV. Dashed red lines are the Dirac conicbands of bulk graphene.

4.1. Tuning external terminals

We first consider both left and right terminals to be exactly extended from the waveguide region to separate the barriers from the terminals physically as displayed in figure 1. The length and width of the graphene ribbon system are respectively set to be $L = 80.7$ nm and $W = 50.4$ nm. The waveguide width is chosen to be $W_G = 10.1$ nm and the applied potential is $\Delta V = -0.25$ eV. There are two reasons for considering the 10.1 nm width waveguide. (a) We are interested in studying the transport on a waveguide with few conducting channels. This might be beneficial in experimental realization since it reduces the scattering among conducting channels and it will enhance the coherent transport. (b) Computational capacity is the other reason. For instance, in our consideration of a 50.4 nm×80.7 nm central region, a general Green's function matrix would roughly have $[(50.4/0.5\sqrt{3}a_0) \times (80.7/3a_0)]^2 \approx (409 \times 172)^2$ elements, where $a_0 = 0.142$ nm is the distance between two atoms. This means that it is unrealistic to consider further larger system setups.

In our study, we have done a series of numerical calculation to explore the possibility of realizing quantized conductance, i.e. vanishing backscattering. In figure 6(a), we set the site potentials in the left and right terminals to be identical, i.e. $V_{L/R} = -0.10$ eV or -0.20 eV. For $V_{L/R} = -0.10$ eV, one can find that the first plateau appears around $G = 1(2e^2/h)$, while for $V_{L/R} = -0.20$ eV, the first plateau becomes roughly to be $G = 2(2e^2/h)$. However, the presence of same site potential on both left and right terminals always gives rise to an oscillating conductance due to the possible mismatch between the terminals and central scattering region. Surprisingly, we find that if the non-zero site potential is only included in one terminal (e.g. left), plateaus, i.e. $G = 1/3/5(2e^2/h)$ arise at different energy intervals (see figure 6(b)). One may ask what would happen to the conductance if V_L and V_R are vanishing? As a sharp comparison, in figure 6(c), we plot the conductance

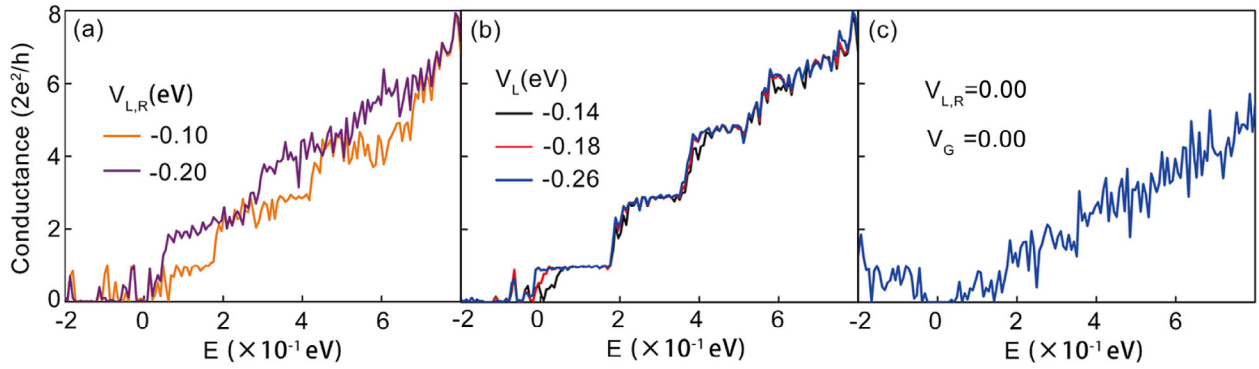

Figure 6. Two-terminal conductance as a function of Fermi energy in a graphene waveguide. (a) The site potentials in both left and right terminals are set to be identical, i.e. $V_L = V_R = -0.10$ eV (orange line) or -0.20 eV (purple line); (b) the site potentials in left and lead terminals are different, i.e. $V_L = 0.14$ eV (black line), -0.18 eV (red line), and -0.26 eV (blue line), with $V_L = 0.00$ eV in right terminal as a reference; (c) the site potentials in both left and right terminals are set to be identical, i.e. $V_L = V_R = 0.00$ eV. Note that: the waveguide is straight. Other parameters are set to be $L = 80.7$ nm, $W = 50.4$ nm, $W_G = 10.1$ nm, $\Delta V = -0.25$ eV, and $V_0 = 0.00$ eV. Both terminals are exactly extended from the waveguide with a width of 10.1 nm.

as a function of Fermi-energy at vanishing site-potentials in both terminals. One can clearly see that the quantized plateaus become oscillating again. This finding emphasizes the importance of the adjustment of site-potentials in both terminals.

4.2. Transport in narrow curved waveguides

Figure 7(a) displays the two-terminal conductance G as a function of Fermi level for a curved waveguide with different bending degrees $D_C = 0.0$, 10.2, 20.4 and 30.6 nm. One can see that for the straight graphene waveguide at $D_C = 0.0$ nm and $E > 0$, the conductance can be approximately quantized to $G = 1,3,5(2e^2/h)$. However, for $E < 0$, the conductance becomes oscillating and always be smaller than $G = 1(2e^2/h)$ due to the strong interference between incoming and back-scattering modes. It is noteworthy to mention that different site potentials of $V_L = -0.22$ eV and $V_R = 0.00$ eV are applied to the left and right terminals to match the waveguide modes. Here, the odd quantized conductance plateau is determined by the incoming modes from the terminals (see dashed lines in figure 7(c)). When the graphene waveguide gradually becomes smoothly curved (see the lower three panels of figure 7(a)), one may expect backscattering is introduced to break the quantization of conductance. To our surprise, the plateau of $G = 1(2e^2/h)$ is not destroyed even at a higher degree of bending (i.e. $D_C = 30.6$ nm), and it becomes even more flat. This striking transport phenomenon reflects precisely the zero bend resistance, which may be attributed to the immunity of the confined waveguides to the variation of the width of side barriers and can pose immediate implications in graphene-based low-power electronics. The conductance is varying in discrete quanta of $2(2e^2/h)$ in figure 7(a) for second and third plateaus. This indicates the possible valley polarization of conductance due to the imbalanced contribution from different valleys K and K'.

In figure 7(b), as an example, we plot the local density of states of the perfectly conducting confined waveguide mode of $G \sim 1\ (2e^2/h)$ at fixed $E_F = 0.03$ eV and $D_C = 20.4$ nm. One can see that the confined waveguide mode only propagates

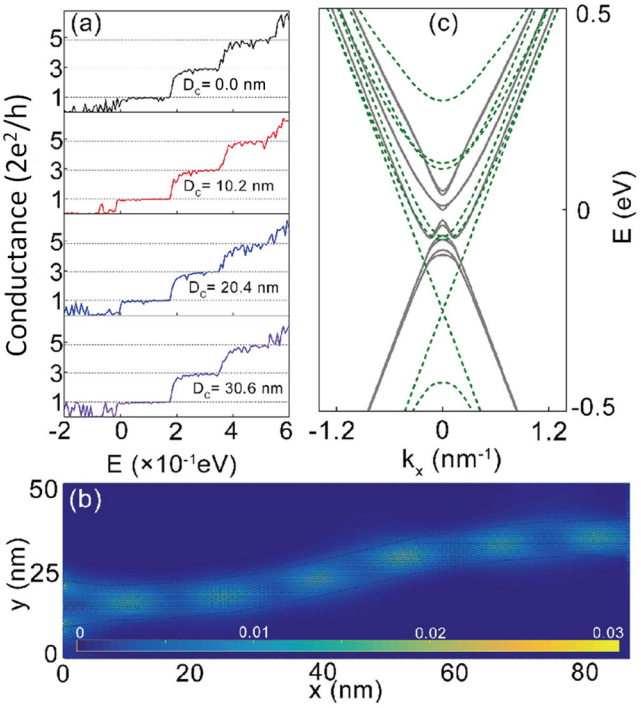

Figure 7. (a) Two-terminal conductance as a function of Fermi level for different curved waveguides, i.e. $D_C = 0.0$, 10.2, 20.4, and 30.6 nm. The system parameters are chosen to be $L = 80.7$ nm, $W = 50.4$ nm, $W_G = 10.1$ nm, and $\Delta V = -0.25$ eV. (b) Spatial distribution of local density of states of the single-mode waveguide. (c) Band matching between the leads (dashed lines) and waveguide area (solid lines) for systems shown in panel (a). Additional on-site potentials of -0.22 eV are added to the leads to align the similar conduction subbands.

locally inside the waveguide. The oscillation peaks on the waveguide are attributed to the traveling wavepackets across the waveguide from the left to right leads. In addition, the number of wavepackets increases at higher Fermi energies, satisfying the plane wave explanation of electron wave function in the transport direction.

Figure 7(c) shows the band matching between the terminals and central scattering region for figure 7(a). As

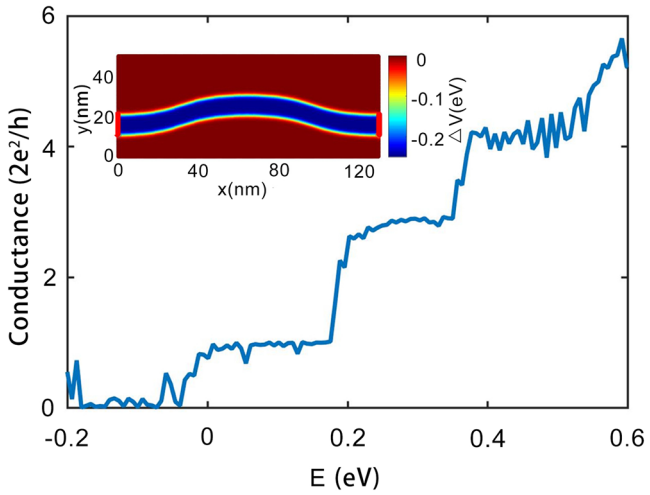

Figure 8. The conductance of a narrow Gaussian-shape graphene waveguide, Inset: smooth edges potential well. Device parameters are $L = 131.1$ nm, $W = 50.4$ nm, $W_G = 10.1$ nm, $\Delta V = -0.25$ eV, $V_0 = 0.00$ eV, $V_L = -0.22$ eV and $V_R = 0.00$ eV.

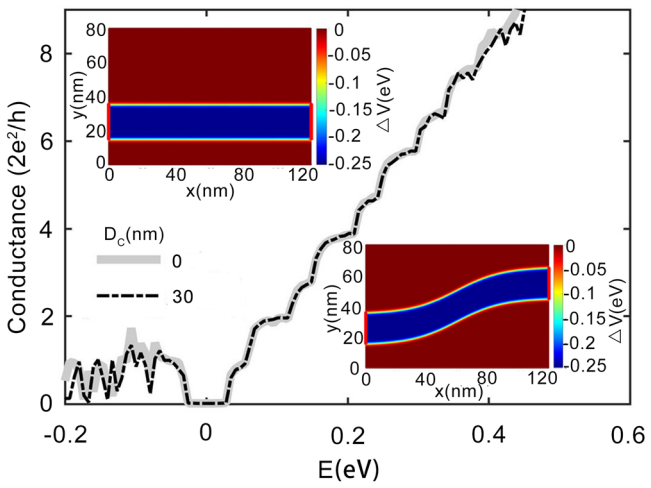

Figure 9. Conductances of a medium size graphene waveguides with smooth edges potential well, see inset figures. Device parameters are as follow $L = 121.0$ nm, $W = 80.7$ nm, $W_G = 20.2$ nm, $\Delta V = -0.25$ eV, $V_0 = 0.00$ eV, $V_L = -0.24$ eV and $V_R = 0.00$ eV. The solid gray line for straight waveguide and dashed black line for curved waveguide $D_C = 30.3$ nm.

mentioned, additional site potentials of -0.22 eV and 0.00 eV are respectively added to the terminal's Hamiltonian to align to similar conduction subbands. For a specific system parameters, careful adjustment of V_L and V_R should be adopted to achieve smooth conductance plateaus, i.e. leads should inject and collect electron effectively. Furthermore, nearly identical conductances at different curvature degrees demonstrate the zero bending resistance of the graphene waveguide as a striking physical property of scattering area. With the increase of E_F, the number of bands also increases. The resulting local density of states is no longer perfectly propagating as that in figure 7(b), but accompanying with dispersive distribution over the whole scattering area. However, the restriction of the width of both terminals ensures the full backscattering of the modes spreading in the whole region and only allows the matched propagating modes, giving rise to different ballistic transport plateaus.

We also examined a Gaussian-shape waveguide at a more extended device $L = 131.1$ nm with smooth edges potential well, see figure 8. Relatively similar conductance is achieved. This is in contrary to a recent report claiming an armchair waveguide is incapable of coherent transport [27].

4.3. Transport in wide waveguides

To highlight the effect of the width of the waveguide, we have considered two example of thicker graphene waveguides, $W_G = 20.2$ nm and $W_G = 40.3$ nm. In bandstructure section, we have shown that wider waveguides, with the same amount of potential at the bottom of well, results in more conducting channels with less energy separation. Consequently, It is expecting to have more plateaus with less energy separation. This is confirmed in figure 9 which in there, we have calculated the conductance of medium size graphene waveguide with $W_G = 20.2$ nm. Other parameters are as follows: $L = 121.0$ nm, $W = 80.7$ nm, $\Delta V = -0.25$ eV, $V_0 = 0.00$ eV, $V_L = -0.24$ eV and $V_R = 0.00$ eV. Once again, the conductance of the straight and curved waveguides are almost identical. Therefore, the property of zero bending resistivity is independent of the width of graphene waveguide. The conductances are noticeably smooth at $W_G = 20.2$ nm as compare to $W_G = 10.1$ nm. The conductances are not varying in discrete quanta of $2(2e^2/h)$. Further exploration shows our nanoribbon contacts in figure 9 are semiconductor type nanoribbons while we have used metallic type nanoribbon by far in all of past examples. It is worth mentioning that with 'm' being an integer number, a nanoribbon with an index number of $3m$ or $3m + 1$ is a semiconductor but $3m + 2$ is a metallic nanoribbon.

It is well known that the current state-of-the-art experiment on graphene waveguide [29] utilized a split gate design. The distance between two top gates was about 121.0 nm and the effective channel width was estimated to be 65.5 nm. Although it is impossible to produce 10.1 nm or 20.2 nm wide lithographic top gates in a realistic device fabrication, one can turn to apply special high-resolution etching techniques [28]. Thus, we performed the transport study on a straight graphene waveguide with $W_G = 40$ nm. Results have been plotted in figure 10 and rest of parameters are as follows: $L = 121.0$ nm, $W = 100.8$ nm, $\Delta V = -0.25$ eV, $V_0 = 0.00$ eV, $V_L = -0.24$ eV and $V_R = 0.00$ eV. In figure 10, the solid gray line is the conductance for the contact being exactly extended from the central waveguide; while the dark dashed line represent the conductance for the width of contact being decreased by 6% (20 atoms) symmetrically. In both cases, the nanoribbon contacts are semiconductors. Fading Plateaus are observable, but the energy range for constant conductances (flat areas) is reduced. This can be attributed to a small energy difference between energy channels, see figure 5(a). In addition, small flat areas of conductance are connected via incomplete vertical lines, see figure 10. Such a smooth rising can be attributed to the higher curvature of conducting subbands of a wide waveguide, compared with the conducting bands of

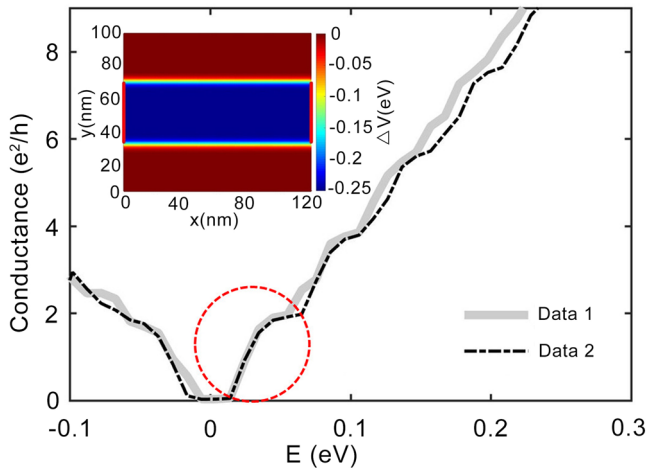

Figure 10. The conductance of a wider $W_G = 40.3$ nm and straight graphene waveguide with semiconductor type contacts. Rest of device parameters are as follows: $L = 120$ nm, $W = 100.8$ nm, $\Delta V = -0.25$ eV, $V_0 = 0.00$ eV, $V_L = -0.24$ eV and $V_R = 0.00$ eV. Inset figures show the structure of waveguides. Smoothness is included and color bar shows the on-site potentials.

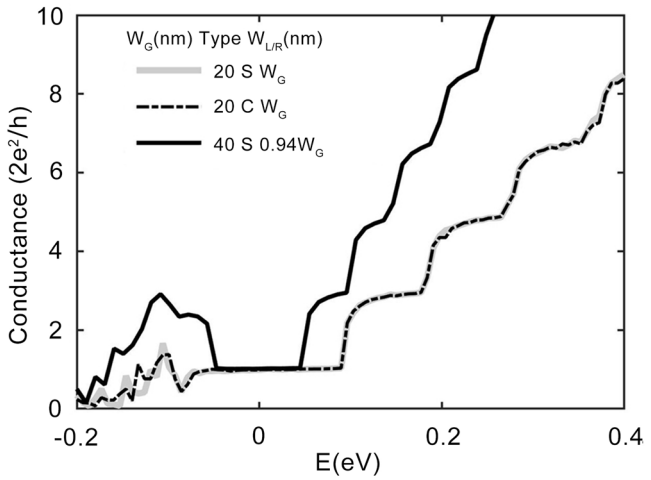

Figure 11. Conductance of two medium sizes $W_G = 20.2$ nm waveguides and a much thicker $W_G = 40.3$ nm straight graphene waveguide with metallic terminals. For $W_G = 20.2$ nm waveguides we have used the parameters of figure 9 and for single $W_G = 40.3$ nm waveguide we have applied the parameters from figure 10, the case of reduced size. 'S' and 'C' refer to straight and curved waveguides respectively.

a narrow graphene waveguide. In other word, higher effective mass gives rise to resistivity and leads to a slope between each semi-flat plateaus. Our results agree well with the recent experimental reports [29]. We also observed that decreasing the width of the contacts has a destructive influence on the conductance of a narrow waveguide. When the width of contacts in a waveguide with WG = 10.1 nm is reduced by 25% (about 20 atoms), then the resulting conductance of this waveguide becomes fluctuating, similar to that shown in figure 6(c). As a comparison, in figure 10, we show that a wider waveguide is more immune to the lead-waveguide mismatch.

To better understand the conductance of the wider graphene waveguides, we also plot three other conductances with metallic terminals in figure 11. To make the terminals metallic, we only decrease two atoms in contacts or reduce the index number by one. For example, we choose a straight and a curved $W_G = 20.2$ nm waveguides, and a $W_G = 40.3$ nm waveguides with reduced size contact (i.e. $W_{L,R} \approx (1\%-6\%)W_G$). The solid gray line and dashed dark line represent the conductance of straight and curved $W_G = 20.2$ nm waveguide, respectively. Other system parameters are identical to those for figure 9. Similarly, we chose the parameters of reduced size terminals in figure 10 to calculate the conductance of $W_G = 40.3$ nm waveguide with metallic contacts as shown in a solid dark line. Again, one can see that the conductance becomes quantized to be $G = 1,3,5,...(2e^2/h)$. Therefore, valley degenerate conductance can be preserved, provided that contacts are metal. Moreover, zero bending resistivity is maintained similar to the conductance in the $W_G = 20.2$ nm waveguides with non-metallic contacts. Comparison between the conductances of two $W_G = 20.2$ nm waveguides and one $W_G = 40.3$ nm waveguide in figure 11 clarifies how denser waveguide's modes in $W_G = 40.3$ nm system leads to more plateaus in the same range of Fermi energy.

It is noteworthy that the interplay between the width of waveguide and the on-site potential plays crucial role in the formation of the valley transport. Moreover, The effect of nonzero temperature can be justified on conductance via so-called broadening function [34]. At the higher temperature, the plateaus are expected to gradually disappear similar to what is observed on the ballistic transport of quantum point contacts, defined in the two-dimensional electron gas (2DEG) of a high-mobility GaAs/AlGaAs heterojunctions [36].

5. Summary

To conclude, we theoretically investigate the electronic transport properties of the confined waveguide modes in curved graphene waveguide. We first systematically study the dependence of the confined waveguide mode on different system geometric parameters and applied gate potentials. We find that the width and symmetry of the side barriers do not affect the bands of the confined waveguide modes, which is a hallmark for the possible ballistic transport in a graphene waveguide with a random but smoothly varying bending. Furthermore, the electronic transport calculation gives direct evidence of nearly quantized conductance in curved graphene waveguide. Such a striking zero bend resistance property makes graphene waveguide an ideal platform to design dissipationless or low-power electronic devices.

Acknowledgments

This work was financially supported by the National Key Research and Development Program (Grant No. 2016YFA0301700), NNSFC (Grant Nos. 11625419 and 11474265), and the China Government Youth 1000-Plan Talent Program. The Supercomputing Center of USTC is gratefully acknowledged for high-performance computing assistance. This was also supported by Chinese Academy of

Sciences and The World Academy of Science for the advancement of science in developing countries.

VM and KW contributed equally to this work.

ORCID iDs

Zhenhua Qiao https://orcid.org/0000-0003-2792-5110

References

[1] Novoselov K S, Geim A K, Morozov S V, Jiang D, Zhang Y, Dubonos S V, Grigorieva I V and Firsov A A 2004 *Science* **306** 666
Novoselov K, Geim A K, Morozov S, Jiang D, Katsnelson M, Grigorieva I, Dubonos S and Firsov A 2005 *Nature* **438** 197
[2] CastroNeto A H, Guinea F, Peres N M R, Novoselov K S and Geim A K 2009 *Rev. Mod. Phys.* **81** 109
[3] Young A F and Kim P 2009 *Nat. Phys.* **5** 222
[4] Lalmi B *et al* 2010 *Appl. Phys. Lett.* **97** 223109
Liu C-C, Feng W and Yao Y 2011 *Phys. Rev. Lett.* **107** 076802
Vogt P *et al* 2012 *Phys. Rev. Lett.* **108** 155501
Chen L *et al* 2012 *Phys. Rev. Lett.* **109** 056804
Pan H *et al* 2014 *Phys. Rev. Lett.* **112** 106802
[5] Xiao D *et al* 2012 *Phys. Rev. Lett.* **108** 196802
Zeng H-L *et al* 2015 *Chem. Soc. Rev.* **44** 2629
[6] Geim A K and Kim P 2008 *Sci. Am.* **298** 90
[7] Katsnelson M, Novoselov K and Geim A 2006 *Nat. Phys.* **2** 620
[8] Dragoman D 2010 *J. Opt. Soc. Am.* B **27** 1325
[9] Beenakker C, Sepkhanov R, Akhmerov A and Tworzyd lo J 2009 *Phys. Rev. Lett.* **102** 146804
[10] Cheianov V V, Fal'ko V and Altshuler B 2007 *Science* **315** 1252
[11] Lee G-H, Park G-H and Lee H-J 2015 *Nat. Phys.* **11** 925
[12] He Y, Ding M, Yang Y and Zhang H 2015 *Superlattices Microstruct.* **85** 761
[13] Hartmann R R and Portnoi M 2014 *Phys. Rev.* A **89** 012101
[14] Myoung N, Ihm G and Lee S 2011 *Phys. Rev.* B **83** 113407
[15] Hartmann R R, Robinson N and Portnoi M 2010 *Phys. Rev.* B **81** 245431
[16] Wu Z 2011 *Appl. Phys. Lett.* **98** 082117
[17] Zhang F-M, He Y and Chen X 2009 *Appl. Phys. Lett.* **94** 212105
[18] Pereira J M Jr, Mlinar V, Peeters F and Vasilopoulos P 2006 *Phys. Rev.* B **74** 045424
[19] Williams J, Low T, Lundstrom M and Marcus C 2011 *Nat. Nanotech.* **6** 222
[20] Rickhaus P, Liu M-H, Makk P, Maurand R, Hess S, Zihlmann S, Weiss M, Richter K and Schonenberger C 2015 *Nano Lett.* **15** 5819
[21] Bai K-K, Qiao J-B, Jiang H, Liu H and He L 2017 *Phys. Rev.* B **95** 201406
[22] Jiang B-Y, Ni G, Pan C, Fei Z, Cheng B, Lau C N, Bockrath M, Basov D N and Fogler M M 2016 *Phys. Rev. Lett.* **117** 086801
[23] Pedersen J G, Gunst T, Markussen T and Pedersen T G 2012 *Phys. Rev.* B **86** 245410
[24] Williams J and Marcus C 2011 *Phys. Rev. Lett.* **107** 046602
[25] Oroszláany L, Rakyta P, Kormáanyos A, Lambert C J and Cserti J 2008 *Phys. Rev.* B **77** 081403
[26] Rickhaus P, Makk P, Liu M-H, Tóvári E, Weiss M, Maurand R, Richter K and Schöonenberger C 2015 *Nat. Commun.* **6** 6470
[27] Cao S-M, Zhou J-J, Wei X and Cheng S-G 2017 *J. Phys.: Condens. Matter* **29** 145301
[28] Tilke A T, Simmel F C, Lorenz H, Blick R H and Kotthaus J P 2003 *Phys. Rev.* B **68** 075311
[29] Kim M, Choi J-H, Lee S-H, Watanabe K, Taniguchi T, Jhi S-H and Lee H-J 2016 *Nat. Phys.* **12** 1022
[30] Marcuse D 1978 *Appl. Opt.* **17** 763
[31] Lewenkopf C H and Mucciolo E R 2013 *J. Comput. Electron.* **12** 203
[32] Gunlycke D and White C 2008 *Phys. Rev.* B **77** 115116
[33] Touski S B and Pourfath M 2013 *Appl. Phys. Lett.* **103** 143506
[34] Datta S 2005 *Quantum Transport: Atom to Transistor* (Cambridge: Cambridge University Press)
[35] Sancho M L, Sancho J L and Rubio J 1984 *J. Phys. F: Met. Phys.* **14** 1205
[36] van Wees B J, Kouwenhoven L, Willems E, Harmans C, Mooij J, Van Houten H, Beenakker C, Williamson J and Foxon C 1991 *Phys. Rev.* B **43** 12431